Preparation, Testing and Characterization of Doped TiO₂ Active in the Peroxidation of Biomolecules under Visible Light

Revathi Bacsa,[†] John Kiwi,[†] Teruhisa Ohno,[‡] Peter Albers,[§] and Victor Nadtochenko*,[†]

Laboratory of Photonics and Interfaces, Institute of Chemical Sciences and Engineering, Swiss Federal Institute of Technology, Lausanne 1015, Switzerland, Department of Material Science, Faculty of Engineering, Kyushu Institute of Technology, 1-1 Sensuicho, Tobata, Kitakyushu 804-8550, Japan, and Electron Microscopy, AQura GmbH, Rodenbacher Chaussee 4, D-63457 Hanau, Germany

Doped TiO₂ samples using different preparative procedures were synthesized using either urea or thiourea leading to N- or S-doped TiO₂. Photocatalytic peroxidation and oxidation (mineralization) of phosphatidylethanolamine (PE) lipid with doped TiO₂ were carried out under light irradiation $\lambda > 410$ nm. The formation of conjugated double bonds in PE molecules was followed to detect the formation of peroxy radicals (peroxidation index) under light excitation ($\lambda > 410$ nm) when doped TiO₂ was used. The kinetics of CO₂ production was monitored during the mineralization of PE. Colored TiO₂ powders were studied in detail by different and complementary physicochemical techniques. The band gap energies of colored TiO₂ were determined by diffuse reflectance spectroscopy (DRS). The visible absorption shoulder of TiO₂ was observed to follow Urbach's law. The variation of the transient decay after 354 nm laser pulse excitation does not correlate with the different N− and S−TiO₂ doping levels introduced by the addition of urea or thiourea. This suggests that the states (recombination centers or traps) introduced by the doping are not effective in varying the decay kinetics within the nanosecond and microsecond time scale. Elemental analysis shows comparable amounts of S- and N-doping of TiO₂ when thiourea is used as dopant. X-ray diffraction reveals no rutile in S−TiO₂ samples heated to 600 °C, suggesting that the addition of sulfur precludes rutilization during sample crystallization. X-ray photoelectron spectroscopy (XPS) of the S−TiO₂ samples confirms the preferential localization of S on the 20 topmost layers of S−TiO₂ upon calcination at 500 °C for 2 h.

Introduction

TiO₂ with photocatalytic activity in the visible range is a research topic of great importance in view of the applications in energy storage and environmental pollution control. Activity under visible light would make possible the indoor use of TiO₂ and applying diffuse light excitation. A large number of techniques have been employed to synthesize TiO₂ powders photoactive in the visible range.[1−17] Recently, doped TiO₂ has been synthesized by reacting TiO₂ powder or a TiO₂ colloidal precursor with urea (from now on N−TiO₂) or thiourea (from now on S−TiO₂).[7,8,18] Doped titania powders have been used in the photocatalytic oxidation of organic molecules or to carry out dye photoinduced decoloration.[1,3,4,7−9] The photokilling of harmful pathogens by TiO₂ under UV-A light has been recently reported[19−23] as well as the peroxidation of the cell membrane of *E. coli* during TiO₂ photocatalysis under UV-A light.[24] The bactericidal action of TiO₂ in indoor applications is associated with the use of the full visible spectrum.

The peroxidation activity of biomembranes by N- or S-doped TiO₂ has not been investigated in detail. This is the object of this study involving nanotechnology and microbiology. Our aim is to optimize the preparation of N- and S-doped powders to be used in the peroxidation of L-α-phosphatidylethanolamine (L-α-cephaline, PE). Nanocrystalline yellow TiO₂ powders have been synthesized, by different methods, leading to materials with a large surface area. PE is one of the main components of the

outer wall membrane and cytoplasmic membrane in gram-negative bacteria.[25] Moreover, PE is a suitable biomolecule for the study of the peroxidation process. PE contains an olefinic H atom in the polyunsaturated fatty acid tail that undergoes a thermodynamically favored peroxy radical attack. Doped TiO₂ large surface area powders with visible absorption were synthesized by several techniques and characterized by diffuse reflection spectroscopy (DRS), attenuated total reflection Fourier transformed infrared spectroscopy (ATR-FTIR), Raman scattering spectroscopy, X-ray diffraction, X-ray photoelectron spectroscopy (XPS), elemental analysis (EA), porosity measurements (BET, pore size), and nanosecond-laser photolysis.

Experimental Section

Preparation of Doped TiO₂. The following methods were used for sulfur doped TiO₂ preparation:
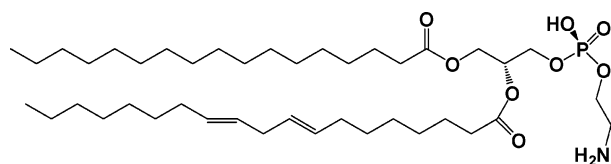
(1) The sol−gel preparation of doped titania colloids was carried out with titanium tetraisopropoxide (Fluka AG, Buchs) as the Ti source and thiourea (Fluka AG, Buchs) as the sulfur source. Both constituents were mixed in ethanol in the ratio 1:4. The resulting slurry was concentrated in a rotavapor and poured into a Petri dish, then inserted into an oven at temperatures 300−550 °C. Thick fumes of sulfur dioxide and foam were observed during combustion leading to the porous TiO₂ powders. The samples were heated for 2 h at 550 °C and 8 h in the case of 350 °C, rendering yellow powders that were labeled as S−TiO₂.

(2) The N-doped TiO₂ synthesis used urea instead of thiourea applying the same procedure as above. The samples obtained were labeled N−TiO₂.

† Swiss Federal Institute of Technology.
‡ Kyushu Institute of Technology.
§ AQura GmbH.

Doped TiO$_2$ in the Peroxidation of Biomolecules

J. Phys. Chem. B, Vol. 109, No. 12, 2005 **5995**

CHART 1: Chemical Structure of PE

(3) Other S-doped TiO$_2$ samples were prepared according to procedures reported recently.[9] The precursors as in method 1 were mixed in ethanol in the ratio 1:4. The aging of the slurries was carried out over 3 days before heating them to 100 °C to eliminate the excess water and then by heating again for 3 h at 500 °C to introduce the crystallographic structure. These samples are labeled S−TiO$_2$-aged.

(4) S−TiO$_2$ samples with SSA greater than 200 m^2/g were prepared by grinding anatase with thiourea followed by calcination at 400 °C. These samples were labeled S−TiO$_2$-ground.

(5) S−TiO$_2$ samples were also prepared by heating of mixtures of thiourea and anatase provided by Tayca corporation (Japan) with a specific surface area (SSA) of 280 g/m^2. Temperatures from 200 to 900 °C at different calcination times were used. The calcination temperature and time for each S−TiO$_2$ sample are noted, 400 × 8, 550 × 2, and 900 × 1, where the first number corresponds to the temperature (°C) and the second number to the calcination time (h).

TiO$_2$ Degussa P25 powder was used as a reference for undoped TiO$_2$ samples.

Sample Preparation for Irradiation Experiments. PE (L-α-phosphatidylethanolamine (L-α-cephaline)) from bovine brain (Aldrich, AG Buchs) was used as received. The chemical structure of PE is shown in Chart 1. PE multilamellar vesicles were prepared by the following procedure: first, a thin dry PE film was spread on the surface of a vessel. The vesicles were stirred in solution (10 mg/mL), with Raschig glass rings under a vigorous flow of N$_2$ gas. As the reaction time progressed, the PE-lipid film transformed into a multilamellar vesicle suspension forming a turbid solution. This suspension was mixed with TiO$_2$ and purged with O$_2$ for 3 min.

Irradiation Procedures. A Suntest solar simulator (from Heraeus AG, Hanau, Germany) illuminator was used with a filter cutoff for wavelengths λ < 410 nm. The filtered light intensity was 45 mW/cm^2 as monitored by a power meter of LSI Corp, Yellow Springs, CO. This value refers to the total radiant light flux in the Suntest cavity. Control experiments were performed applying the full Suntest light (90 mW/cm^2) on Degussa P-25 in the absence of the cutoff filter λ < 410 nm. Suspensions of TiO$_2$ (1 mg/1 mL) and 1 mg/mL of PE in a 10 mL aqueous solution in 40 mL Pyrex reactor vessels were irradiated after purging with O$_2$.

Spectrophotometric Detection of Conjugated Dienes. To measure the rate of formation of conjugated dienes, 100 μL of the vesicle suspension was diluted in 1 mL of H$_2$O. The absorption spectra were measured in a quartz cell with an optical path length of 0.1 cm. Conjugated dienes show a distinct absorption in the UV at 234 nm for the cis isomer (28 000 dm^3 mol^{-1} cm^{-1}) and at 236 nm for the trans isomer (26 000 dm^3 mol^{-1} cm^{-1}). The optical density was monitored at 234 nm to determine the conjugated diene concentration.

X-ray Diffraction. The crystalline phases of the TiO$_2$ samples were determined with a Siemens X-ray diffractometer using Cu Kα radiation

DRS Measurements. Ultraviolet−visible diffuse reflectance spectra of TiO$_2$ powders were measured with a Cary 5 spectrophotometer provided with a diffuse reflectance accessory.

The Kubelka−Munk relations measuring K/S for thick samples were used to convert reflectance measurements (R) into the equivalent absorption spectra. K and S are the absorption and scattering coefficients of TiO$_2$. The reflectance of MgO was used as reference $(R_{MgO})^{26}$

$$R_\infty = \frac{R}{R_{MgO}} \tag{1}$$

$$\frac{K(\lambda)}{S(\lambda)} = \frac{(1 - R_\infty)^2}{2R_\infty} \tag{2}$$

Attenuated Total Fourier Transform Infrared Spectroscopy. ATR-FTIR spectra were measured in a Portmann Instruments AG spectrophotometer equipped with a Specac attachment (45° one pass diamond crystal). The spectra obtained after 64 scans with a 4 cm^{-1} resolution in the spectral range of 400−5000 cm^{-1} were stored for analysis.

Raman Spectroscopy. Raman spectra of S−TiO$_2$ samples were recorded at room temperature using a Micro-Raman setup (DILORXY), backscattering geometry and at λ = 488 nm (3−5 mW). A well-dispersed suspension of the sample was placed on a glass slide and allowed to dry before taking the Raman spectrum.

Laser Photolysis of Doped TiO$_2$ Powders. Laser photolysis experiments were carried out using the light pulses at λ = 354 nm wavelength (third harmonic) of the Nd^{3+} YAG laser. The duration of the laser pulse was 12 ns with a power of 0.1 mJ/pulse. Experiments were performed in the diffuse reflectance mode using an optical fiber for the collection of the diffuse scattered light. The intensity of the reflected light was monitored with a monochromator (Applied Optics) and the signals were stored in a digital oscilloscope (Tektronix TDS 640) for further processing.

X-ray Photoelectron Spectroscopy (XPS). The XPS measurements were performed using Mg Kα radiation at a power of 150 W. The electron energy analyzer (Leybold EA 11A) was operated at a pass energy of 75 eV in the fixed analyzer transmission mode. The binding energy scale of the spectrometer was referenced to the Au 4f$_{7/2}$ signal of the SCA A83 standard of the National Physics Laboratory (NPL, Teddington, U.K.) at 84.0 eV. A DS100 set was utilized to evaluate the XPS data with standard routines (subtraction of X-ray satellites, Shirley-type background subtraction, corrected by the relative sensitivity factors). The presence of electrostatic charging effects was controlled by additional measurements including charge compensation by changing the electrostatic potential at the entrance aperture of the electron energy analyzer. The sputtering of the doped TiO$_2$ catalysts was carried out with 5 keV Ar ions.

Results and Discussions

X-ray Diffraction. The crystal structure of the yellow TiO$_2$ samples was determined using X-ray powder diffraction. Figure 1 shows the X-ray diffractograms of S−TiO$_2$ prepared by heating the mixture of anatase with thiourea in air at different temperatures. All the samples except those heated to 900 °C show only the anatase phase. It was surprising to find that the sample heated to 900 °C contained a significant fraction of anatase because the transition temperature of anatase to rutile is around 700 °C. Inhibition of grain growth seems to occur due to the presence of sulfur in the grain boundaries, preventing the phase transition of anatase to rutile.

Lattice parameters were measured using NaCl as an internal standard and do not reveal any significant change in S−TiO$_2$
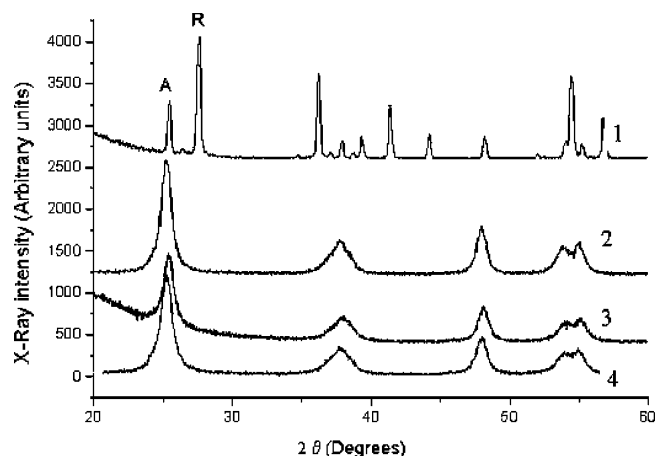
Figure 1. X-ray diffractograms for samples of S−TiO₂: (1) S−TiO₂ 900 × 1; (2) S−TiO₂ 500 × 2; (3) S−TiO₂ 420 × 2; (4) S−TiO₂ 350 × 9.
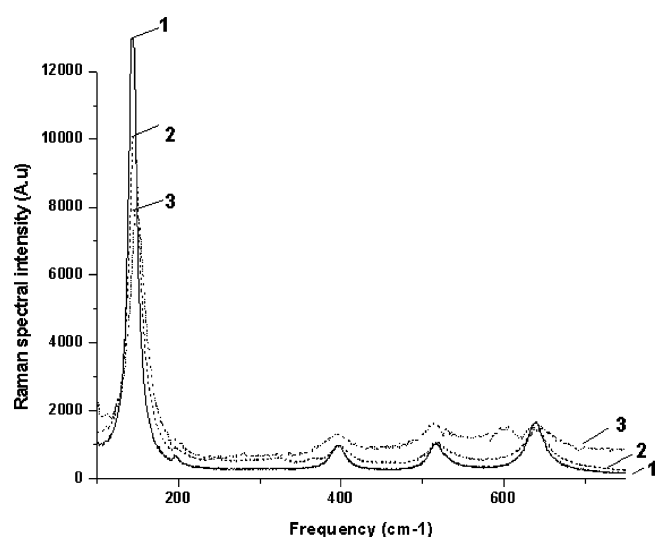
Figure 2. Raman spectra of S−TiO₂ samples: (1) S−TiO₂; (2) S−TiO₂ aged; (3) S−TiO₂ ground.

anatase compared with pure anatase. Elemental analysis found sulfur levels below 1.5% for the samples shown in Figure 1. But a rutile phase was observed for samples treated under similar conditions with urea instead of thiourea. The thiourea treatment seems to preclude the formation of rutile even at 900 °C by incorporating sulfur into anatase. This is confirmed by the results reported in Figure 8a obtained by XPS sputtering of the S−TiO₂ sample. It can be suggested that the higher sulfur concentration in the grain boundaries with respect to the bulk TiO₂ leads to a slower grain growth hindering rutile formation.

Raman Spectroscopy. Raman spectra of S−TiO₂ samples prepared by different synthesis techniques are shown in Figure 2. The spectra show predominantly the anatase phase. The position and width of the E_g mode at 144 cm^{-1} is different for the different samples. The broadest bandwidth was observed for the S−TiO₂ ground sample. The E_g mode at 144 cm^{-1} was found to be sensitive to crystallite size[27,28] in the case of anatase. Not only was a shift observed in the position of the E_g but the full width at half-height was also found to increase with decreasing crystallite size. Bersani et al.[27] have plotted the fwhm values as a function of the crystallite size calculated from XRD. Using the calibration in ref 27, we determined a crystallite size around 5 nm for the S−TiO₂ ground sample. This value agrees with the value found by electron microscopy. Parker and Siegel[28] have observed the shift and broadening of the Raman spectra

with respect to samples having nonstoichiometric oxygen. Oxygen vacancies will be discussed below.

ATR-FTIR Spectroscopy of N− and S−TiO₂ Samples. Figure 3 shows the ATR-FTIR spectra of N− and S−TiO₂ prepared by different methods. The peak observed at 1635 cm^{-1} is due to the adsorbed water. The shoulder beginning below 1000 cm^{-1} corresponds to the titania crystal lattice vibrations. Spectrum 1 of S−titania (physical mixture of TiO₂ with thiourea with subsequent heating) shows several peaks in the region 1600−1200 cm^{-1}. If this sample is heated for 30 min in an O₂ atmosphere, the peaks almost disappear, suggesting that these peaks originate from thiourea traces left during the sample preparation. Spectrum 2 does not show residual thiourea peaks. The heating at 475 °C in an O₂ flow leads to the complete oxidation of that residual thiourea. Two peaks near 1120 cm^{-1} (assigned to SO_4^{2-}) and 1047 cm^{-1} are seen in spectrum 2. Spectra 3, 4 and 5 relate to titania samples employing TTIP sol−gel and thiourea and show peaks of 1120 and 1047 cm^{-1}. Spectra 3 and 4 show that heating samples for 30 min in O₂ flow does not lead to the disappearance of these peaks. These peaks were not observed in the case of N−TiO₂ samples prepared with urea as shown in spectrum 6. Due to the high temperature used during the calcination of the S−TiO₂ 900 × 1sample, the peaks at 1120 cm^{-1} and 1047 cm^{-1} were not observed in spectrum 7. Heating at 500 °C in the air atmosphere removed these peaks. Spectrum 8 corresponds to a sample that was thoroughly washed with respect to the samples 3, 4 and 5.

Surface Area of Doped TiO₂ Samples. The photocatalytic activity of TiO₂ is known to be a function of its surface properties and increases with the SSA of the samples used. During this study, we focused on the preparation of doped TiO₂ using a low-temperature route to achieve TiO₂ powders with a large SSA. The porosity and SSA data are shown in Table 1. The N₂ adsorption−desorption isotherms of N− and S−TiO₂ samples are shown in Figure 4. Most of the samples show a type II isotherm with hysteresis loops corresponding to capillary condensation in the TiO₂ mesopores and a limiting gas uptake within the high p/p^0 region. The initial part of the isotherm is attributed to monolayer−multilayer adsorption. The pore size distribution followed the Barrett, Joyner and Halenda (BJH)[29] equation assuming spherical pores.

Figure 4 shows that with the exception of S−TiO₂ 900 × 1, the TiO₂ samples presented a mesoporous type porosity. The forms of the isotherms differ, showing a different pore structure for different TiO₂ samples. The S−TiO₂ sol−gel sample shows a wider hysteresis loop due to the higher pore ordering. The sample S−TiO₂ 500 × 2 shows an isotherm presenting no hysteresis.

The pore size distributions have been calculated using the BJH equation assuming spherical pores in the range 2−500 nm. The samples show a distribution of pores with sizes <10 nm. The sample prepared by physical grinding shows a wider size distribution of pores (Figure 5, trace 3). We suggest that this effect is associated with reduction in grain size due to grinding as presented in Figure 5. The pore size distribution for the S−TiO₂ 500 × 2 shows a fairly monodisperse pore diameter distribution of 5 nm (Figure 5, trace 1). Specific pore sizes may enhance the adsorption of the organic probe interacting more favorably with the chosen substrate.

UV−Vis DRS Spectra of TiO₂ Powders. Figure 6 shows the comparative UV−Vis spectra of doped TiO₂ powders. In the DRS experiments, UV−vis reflectance data cannot be used directly to measure the absorption coefficients because of the large scattering contribution to the reflectance spectra. Normally

Doped TiO₂ in the Peroxidation of Biomolecules

J. Phys. Chem. B, Vol. 109, No. 12, 2005 **5997**
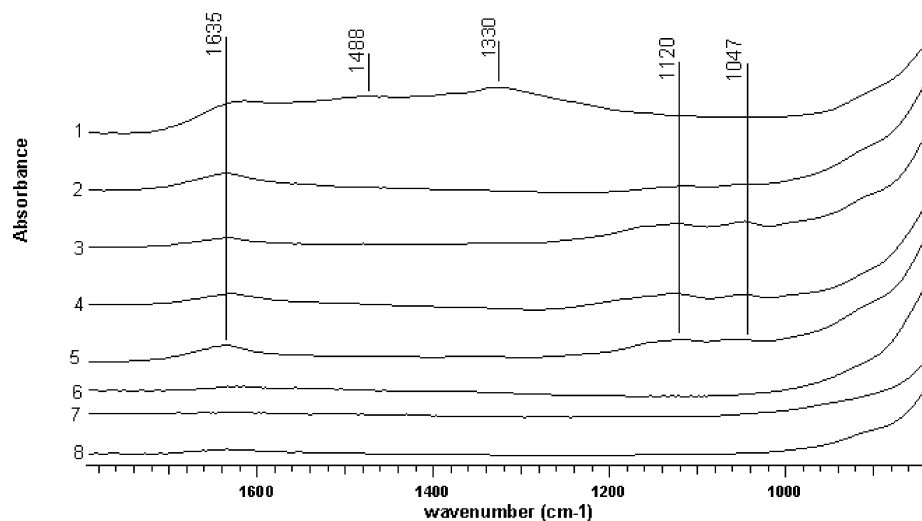
Figure 3. ATR–FTIR spectra of TiO₂ samples: (1) S–TiO₂ ground; (2) S–TiO₂ ground heated for 30 min at 475 °C in O₂; (3) S–TiO₂ 550 × 2; (4) S–TiO₂ 550 × 2 heated for 30 min at 475 °C in O₂; (5) S–TiO₂ 500 × 5; (6) N–TiO₂ sol–gel; (7) S–TiO₂ 900 × 1; (8) S–TiO₂ aged.

TABLE 1: Porosity of Doped TiO₂ Samples

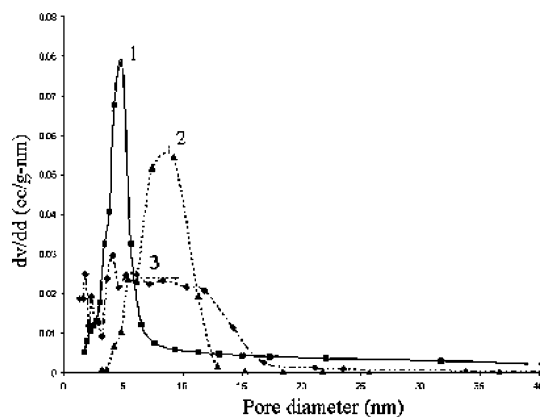|	vol,[a] cm³/g	BET surface area, m²/g	av pore diam,[b] nm
S–TiO₂	0.258	122.3	8.27
N–TiO₂	0.362	167.3	8.39
S–TiO₂ 400 × 8	0.427	183.9	7.37
S–TiO₂ 550 × 2	0.245	106.17	9.09
S–TiO₂ 500 × 4	0.442	160.7	9.33
S–TiO₂ 500 × 2	0.419	139.1	9.73
S–TiO₂ 900 × 1	0.021	5.1	6.67
S–TiO₂-aged	0.431	95.54	17.13
S–TiO₂-ground	0.288	200.3	5.77

[a] BJH desorption cumulative pore volume of pores between 2 and 500 nm diameter. [b] Average pore diameter (4V/A by BET).
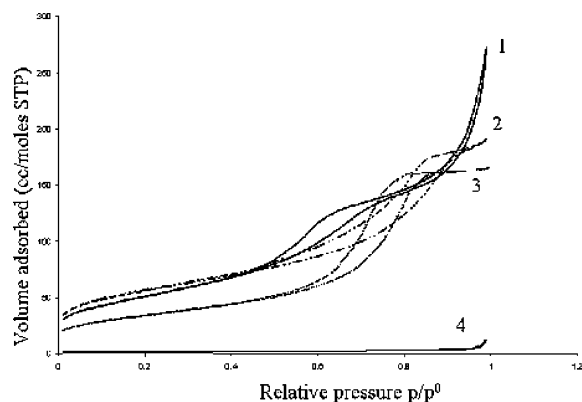
Figure 4. Isotherms of the samples: (1) S–TiO₂ 500 × 2; (2) S–TiO₂ ground; (3) S–TiO₂; (4) S–TiO₂ 900 × 1.

Figure 5. Pore size distribution for the samples: (1) S–TiO₂ 500 × 2; (2) S–TiO₂ sol–gel; (3) S–TiO₂ ground.

it is assumed that there is only a weak dependence of the scattering coefficient S on the wavelength. The value of K/S is assumed to be proportional to the absorption coefficient within the narrow range of energy containing the absorption edge features. Features in the scattering coefficient S may result from a single particle scattering effect. For the comparative studies of TiO₂ powders having similar crystallite size, the effect of particle size on the scattering coefficient is neglected.

The TiO₂ spectra are shown in Figure 6 in four different coordinates. Figure 6a shows the DRS of TiO₂ powders for K/S plots as a function of wavelength. The arrow indicates the appearance of the absorption band $\lambda > 410$ nm for colored TiO₂ samples. The spectral features near 2.85 eV (450 nm) for N- and S-doped TiO₂ are seen in Figure 6d. These features are not observed for Degussa P-25 but are observed for the doped TiO₂ samples. Figure 6d shows the second derivative spectra for some

TiO₂ samples. The spectral features at 2.85 eV indicate a significant change in the joint density of states (JDOS) for the doped TiO₂ samples with respect to the undoped TiO₂. JDOS changes are similar for TiO₂ samples treated by urea or thiourea.

The spectra of the N– and S–TiO₂ samples are shown in Figure 6b in a semilogarithmic plot. Figure 6b) shows that the shoulder of the doped TiO₂ absorption in the visible can be approximated by Urbach's law: $K \propto \exp(\sigma(h\nu - E_g)/kT)$,[30] where σ is a constant, and kT/σ refers to the energy distribution of states below the energy edge E_g. Figure 7a relates to the determination of σ/kT as the slope in the linear fit of the plot of $\ln(K)$ vs $h\nu$. The values of σ/kT for doped TiO₂ samples are shown in Table 2. The lower the value of σ/kT, the wider the energy distribution of states in the semiconductor band edge. It should be mentioned that for the S–TiO₂ and N–TiO₂ samples, the values found for σ/kT coincide. For Degussa P-25 or for the almost white sample S–TiO₂ 900 × 1 h, the values of σ/kT are observed to be about 2.5 times higher than for the doped TiO₂ samples.

The spectra in Figure 6c are used to estimate the band gap values from the DRS data. The crystalline d⁰ metal oxides exhibit indirect absorption edges. The energy dependence of the absorption coefficient for semiconductors near the absorption edge is given by $K \propto \exp(\sigma(h\nu - E_g)^n/h\nu)$, where E_g is the band gap energy.[30] The value of n is $n = \frac{1}{2}$ for direct allowed transitions and $n = 2$ for indirect allowed transitions. The forbidden transitions will not be considered, because the
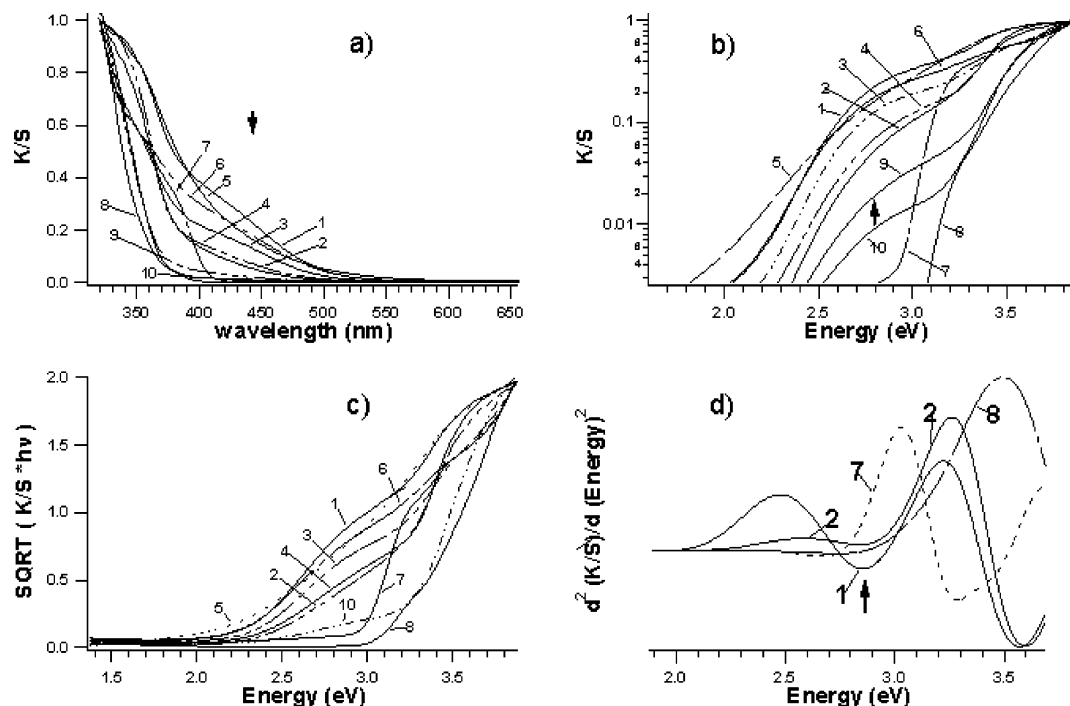
Figure 6. DRS of TiO$_2$ samples. Labels in each panel refer to the sample used: (1) S$-$TiO$_2$ sol$-$gel; (2) N$-$TiO$_2$; (3) S$-$TiO$_2$ 550 × 2; (4) S$-$TiO$_2$ aged; (5) S$-$TiO$_2$ ground; (6) S$-$TiO$_2$400 × 6; (7) S$-$TiO$_2$ 900 × 1; (8) Degussa P-25; (9) S$-$TiO$_2$ 500 × 2; (10) S$-$TiO$_2$ 400 × 8. (a) DRS spectra in coordinates of K/S vs wavelength. (b) Semilogarithmic plot of the K/S vs photon energy. (c) DRS spectra in the coordinates of indirect transitions. (d) Second derivative of DRS spectra.
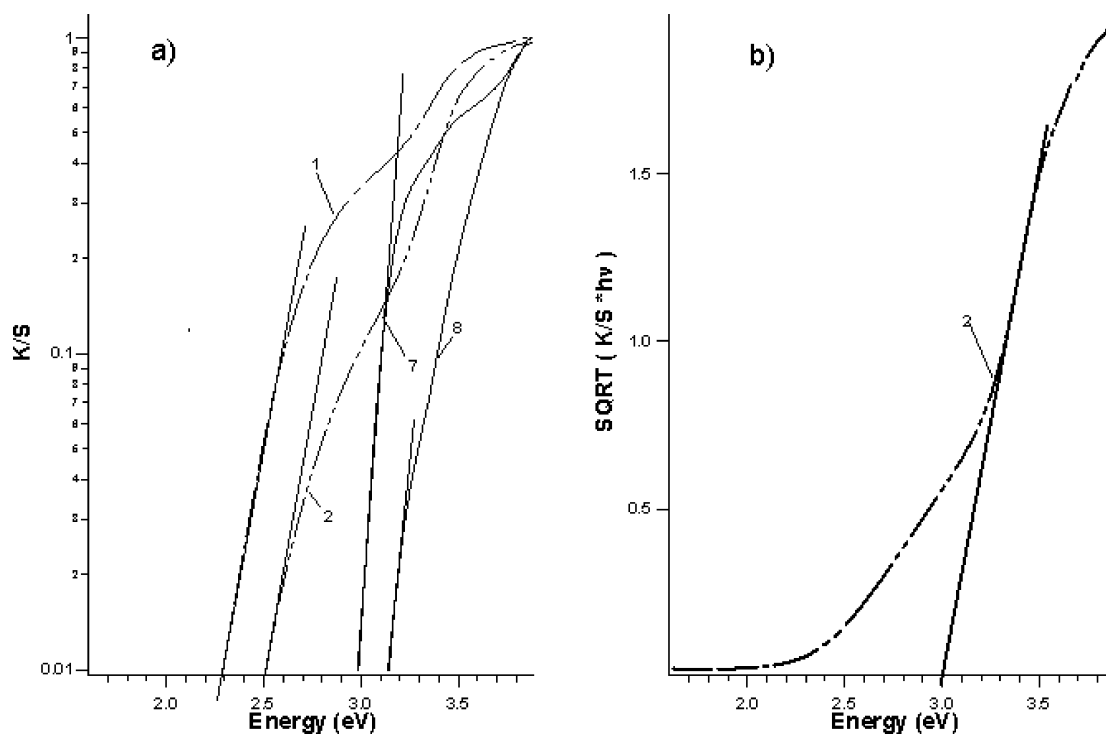
Figure 7. (a) DRS spectra in semilogarithmic coordinates. Linear fits are approximations according to Urbach's law. (b) DRS spectra showing the indirect optical transition in TiO$_2$. The intercept values of the straight lines with the x-axis are used to estimate the edge of the subbands. Key: (1) S$-$TiO$_2$; (2) N$-$TiO$_2$; (7) S$-$TiO$_2$ 900 × 1; (8) Degussa P-25.

transitions forbidden by symmetry rules have a low probability of occurring. The band gaps for small crystalline size semiconductor particles depend on particle size only when the exciton Bohr radius $a_B = \epsilon\hbar^2/m_e^* e^2$ is comparable to or lower than the particle size. Rutile has a static dielectric constant $\epsilon \sim 100$, and an effective mass of $m^* \sim 20m_e$, due to the flat conduction band and also due to polaronic effects.[31-35] Therefore, the Bohr radius for rutile a_H is close to 2.6 Å. The static dielectric constant

of anatase is $\epsilon \sim 31$, and the effective mass is $m^* \sim m_e$. From this, the value $a_H \sim 15$ Å can be estimated.[31] Both exciton Bohr radii of rutile and anatase are substantially smaller compared to the particle size of these powders. The effect of the quantum confinement on the energy edge position can be neglected.

The E_g value was estimated for the intrinsic absorption of TiO$_2$. The linear fit for the dependence SQRT($K/S* h\nu$) vs $h\nu$ was used in the vicinity of the main TiO$_2$ absorption as shown

TABLE 2: σ/kT Values (from DRS Measurements)

| samples	σ/kT (eV^{-1})
S–TiO₂	7.69 ± 0.032
N–TiO₂	7.64 ± 0.064
S–TiO₂ 400 × 6	6.94 ± 0.044
S–TiO₂ 400 × 8	4.72 ± 0.021
S–TiO₂ 550 × 2	7.53 ± 0.061
S–TiO₂ 500 × 2	5.20 ± 0.061
S–TiO₂ 900 × 1	19.5 ± 0.21
P-25	18.07 ± 0.38
S–TiO₂ aged	6.85 ± 0.058
S–TiO₂ ground	5.09 ± 0.007

TABLE 3: Band Gap Energies Determined from the Optical Absorption Spectra by the Formula of Indirect Allowed Transitions

samples of TiO₂	E_g (eV)
S–TiO₂ (sol–gel 400 × 2)	2.65
N–TiO₂ (sol–gel 400 × 2)	2.99
S–TiO₂ 400 × 8	3.18
S–TiO₂ 400 × 6	2.95
S–TiO₂ 550 × 2	2.73
S–TiO₂ 500 × 2	2.92
S–TiO₂ 900 × 1	3.00
degussa TiO₂ P-25	3.18
S–TiO₂ aged	3.04

Figure 7b for the N–TiO₂. The intercept of the *x*-axis in the Figure 7b is the value of E_g, and is estimated from the *x*-axis intercept of the linear fit for the curves in Figure 6c. The E_g data are shown in the Table 3. The value of E_g for Degussa P-25 is found to be 3.18 eV and coincides with the E_g value for anatase. This is the expected because 80% of Degussa P-25 consists of anatase. Table 3 shows lower values of E_g for N- and S-doped TiO₂ samples.

Elemental Analysis. Elemental analysis shows the presence of both N and S in the TiO₂ samples treated with thiourea. S atoms were not present in TiO₂ treated by urea. S–TiO₂ 400 × 6 1.08% N and 1.32% S. S–TiO₂ 500 × 2 0.13% N and 0.73% S. S–TiO₂ 0.03% N and 0.62% S. N–TiO₂ 0.18% N and 0% S. S–TiO₂-aged 0.26% N and 0.28% S. This elemental analysis determines the overall content of an element in the doped TiO₂ particles. In the section below, the XPS sputtering of the S–TiO₂ samples shows that the dopant S is localized in the boundary region of the TiO₂ particles (Figure 8a). This spatial S distribution controls the crystallographic properties of the S–TiO₂ sample as mentioned previously in the X-ray diffraction section.

X-ray Photoelectron Spectroscopy (XPS). The sample S–TiO₂ 500 × 2 active in PE photodegradation had a surface composition of 7.3% C(1s), 1.02% N(1s), 70.9% O(1s), 1.88% S(2p) and 18.9% Ti(2p). The C content originates from the organic impurities of the reagents and from the atmospheric CO₂ during the preparation of S–TiO₂. The N content found in the S–TiO₂ samples comes from the thiourea employed during the preparation of S–TiO₂. The N–TiO₂ 400 × 2 sol–gel sample had the following composition: C(1s) 19.6%, N(1s) 1.17%, O(1s) 61.9%, S(2p) 0% and Ti(2p) 17.4%. The binding energies (BEs in eV) for the S–TiO₂ sample 500 × 2 were as follows: C(1s) 285; N(1s) 401.2; O(1s) 530.5; S(2p) 169.7; Ti(2p) 460.8. For the N–TiO₂ 400 × 2 sol–gel sample the BE values found were as follows: C(1s) 284.9; N(1s) 399.2; O(1s) 530.2; Ti(2p) 460.5. The C, O and Ti and do not vary significantly for samples of S–TiO₂ and N–TiO₂. The BEs of the Ti signal show variations due to specific interactions between TiO₂ and S or N and the TiO₂ compound during the sample preparation.
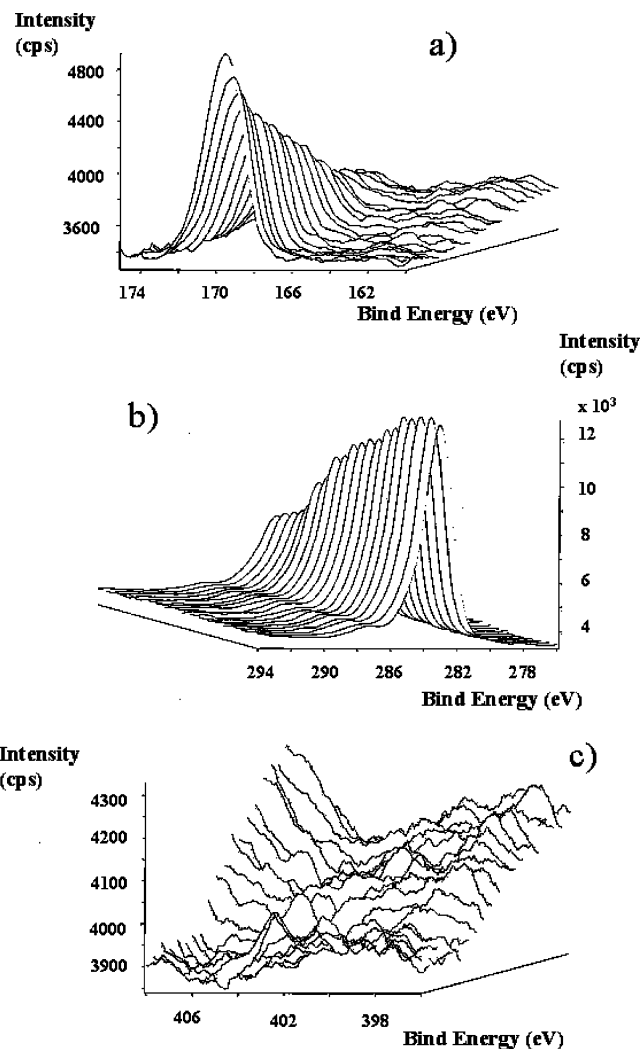

Figure 8. (a) Ar ion sputtering of S–TiO₂ sample showing the decrease of S contents in the catalyst as the distance from the surface increases. (b) Ar ion sputtering of S–TiO₂ sample showing the decrease of C contents in the catalyst as the distance from the surface increases. (c) Ar ion sputtering of S–TiO₂ sample showing the decrease of N contents in the catalyst as the distance from the surface increases.

The sputtering with Ar ions enables us to find the depth profile of the elements in the 20 topmost layers of the S–TiO₂ catalyst and shows the localization of S on the TiO₂ topmost layers in Figure 8a. This S distribution may be responsible for the anti-rutilization effect observed during the preparation of these catalysts. Figure 8b shows the presence of C in the same sample due to the atmospheric CO₂ present during the preparation of this catalyst. Figure 8c shows that several peaks of N species corresponding to diverse N species are distributed evenly within the sample topmost 20 layers. The peaks around 397–399 eV correspond to the presence of amino functional groups. Peaks around 400 eV show the presence of ammonia groups. The less oxidized NO$_x$ species (x < 2) show some peaks around 402 eV, followed by NO₂⁻ peaks (402–403 eV) and NO₃⁻ peaks (407–408 eV). The O and Ti level in the 20 topmost layers did not vary in the S–TiO₂ catalyst as determined by sputtering experiments.

The sputtering of the N–TiO₂ sol–gel 400 × 2 up to 20 layers deep revealed a stable level of O, Ti, C and N species. The N species presented a very similar distribution of peaks as shown in Figure 8c for S–TiO₂. This implies again the existence of several N oxidation states in this catalyst.

Photodynamics of Doped TiO₂ Charge Carriers within
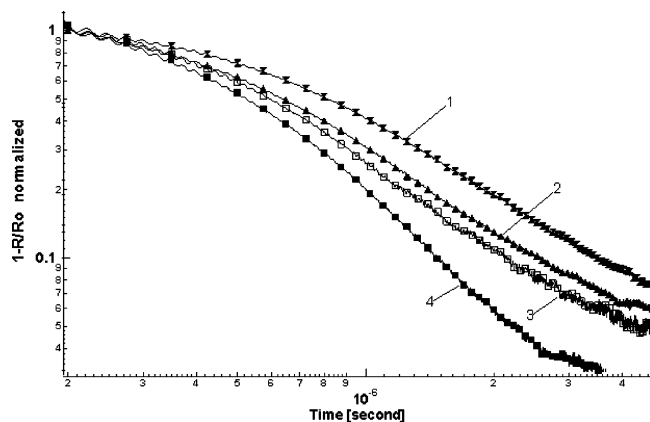
Figure 9. Dynamics of transients decay for the colored TiO_2. Excitation $\lambda = 354$ nm. Probe wavelength is 700 nm. Key: (1) $N-TiO_2$ sol−gel; (2) $S-TiO_2$ aged; (3) Degussa P25; (4) $S-TiO_2$ ground.

the Microsecond and Nanosecond Time Scales. Figure 9 shows the transient decays observed by kinetic laser spectroscopy for N− and $S-TiO_2$ samples. The laser excitation photogenerates the electron transition from the TiO_2 valence band. The probe wavelength for the transient at 700 nm was close to the spectral band of the electron photogenerated by TiO_2. The transient decay plotted in Figure 9 is a stretched-exponential decay shown in a log−log plot. The decay kinetics of N− and $S-TiO_2$ samples were observed to be similar for different N- or S-doping levels. The variation of the transient decay does not correlate with the different N− and $S-TiO_2$ doping levels used when either urea or thiourea is added. Therefore, the method of preparation (sol−gel or mechanical mixing) affects the transients in a more important way than the doping of TiO_2 either by N or S.

$S-TiO_2$ Samples Leading to Double Bond Conjugation of PE. The production of HOO• or ROO• radicals with a polyunsaturated fatty acid tail of lipids is thermodynamically favored. It occurs due to the abstraction of an olefinic H atom. The molecular rearrangement of L (L = unsaturated chain in Scheme 1) leads to the double conjugation. Rearrangement of the double bond stabilizes the lipid radical, and in the presence of the O_2, the production of hydroperoxides was observed. When the lipid acyl chain contains more than one double bond, lipid oxidation leads to the formation of conjugated double bonds. The peroxidation index with the conjugated double bond formation was followed to monitor the formation of HOO• (OO•− radicals in net sense).[28]

The increase in the intensity of the absorption band at 234 nm in Figure 10 provides the proof for the conjugated double bonds formation during the $S-TiO_2$ mediated photocatalysis in aqueous dispersion. Suntest solar irradiation was used in conjunction with a light filter $\lambda < 410$. For comparison, the

same reaction was carried out using the full UV−vis output of the Suntest light on TiO_2 Degussa P-25. Similar changes were observed for both systems. We can therefore infer that the same peroxidation products are formed using the $S-TiO_2$ catalyst with light under $\lambda > 410$ nm and using TiO_2 Degussa P-25 under the full Suntest irradiation, which has a UV component corresponding to 5% of the total irradiation down to 300 nm.

Figure 11 shows the kinetics of the conjugated double bond formation. The initial rate of double bond formation with Degussa P-25 TiO_2 (trace 1) under full Suntest light is higher than for Degussa P-25 TiO_2 (trace 6) using a filter for $\lambda < 410$ nm. The $S-TiO_2$ 500 × 2 (trace 2) shows in the presence of a cutoff filter at $\lambda = 410$ nm an activity close to Degussa P-25 TiO_2 (trace 1) after 140 min. Under full Suntest light, TiO_2 Degussa P-25 gives a yield of conjugated double bonds very similar to the former one. Thus, for $S-TiO_2$ (trace 2), the initial reaction rate of double bond conjugation is slower compared to TiO_2 Degussa P-25 (see Figure 11, trace 1). Other $S-TiO_2$ samples in Figure 11 (traces 3, 4, 5, 7) present a lower peroxidation activity than the $S-TiO_2$ 500 × 2 sample.

Measurements of pH before and after the reactions reported in Figure 11 show that the pH decreases from 5.7 to 3.2 when $S-TiO_2$ or Degussa P-25 is irradiated for 10 h under light an using a cutoff filter at 410 nm. When Degussa P-25 was used under full Suntest light, the pH remained constant at 5.7 within the same reaction time. The pH decrease during the reaction with light of $\lambda > 410$ nm is due to the accumulation of carboxylic acids. For TiO_2 Degussa P-25 under the full Suntest irradiation, these carboxylic groups decomposed during the reactions. This observation follows the pattern for the rate of CO_2 formation during peroxidation as shown in Figure 12. The yield of CO_2 is substantially higher under full Suntest light than when $S-TiO_2$ or TiO_2 Degussa P-25 was used in conjunction with a 410 nm filter.

Figure 12 shows the formation of CO_2 due to the peroxidation under visible light. The $S-TiO_2$ $\lambda > 410$ nm is shown to induce a partial PE mineralization reaching only the carboxylic acid formation stage. This is the reaction step preceding mineralization. At the same time, a limited peroxidation is observed using Degussa P-25 at $\lambda > 410$ nm. This shows the involvement of sub-bandgap states[29,30] of un-doped TiO_2 during the photocatalytic peroxidation of PE. For N− or $S-TiO_2$ samples, the sub-bandgap states form a near *continuum* and these states seem to play an important role during visible light induced photocatalysis. [29]

The observation of the conjugation of double bonds during the photodecomposition of PE implies the formation of peroxy radicals under the excitation of colored TiO_2 by visible light ($\lambda > 410$ nm). The common pathway for the peroxy radical formation is the scavenging of photogenerated electrons by O_2. The produced HO_2• radical reacts with PE as shown in Scheme

SCHEME 1: Lipid Peroxidation Due to TiO_2 Photogenerated ROO• in the Presence of O_2
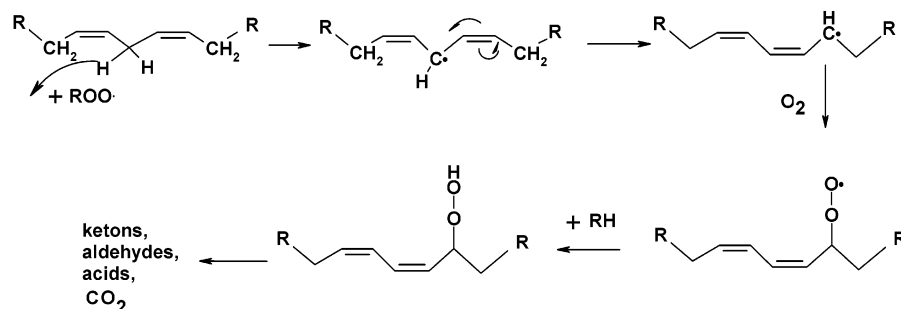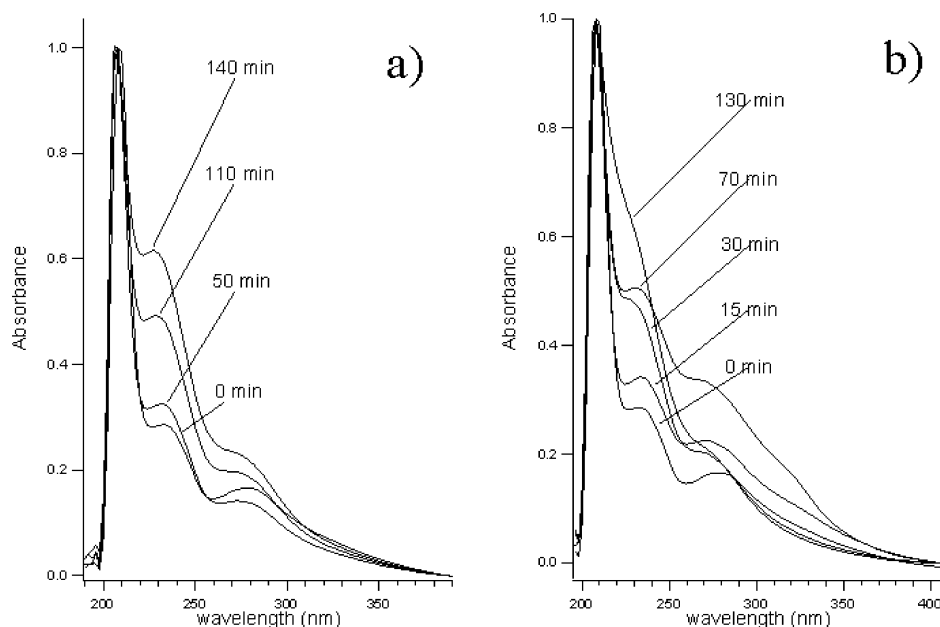
Figure 10. Absorbance spectra changes during photocatalytic peroxidation of PE. Normalization of spectra at $\lambda = 210$ nm. S$-$TiO$_2$ 500 $\times$ 2, $\lambda > 410$ nm.
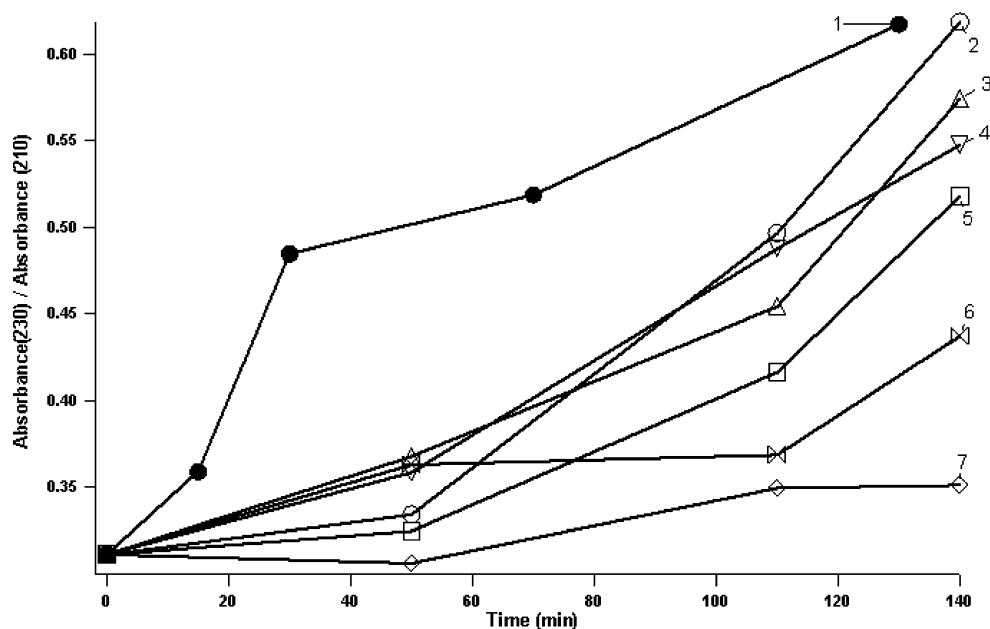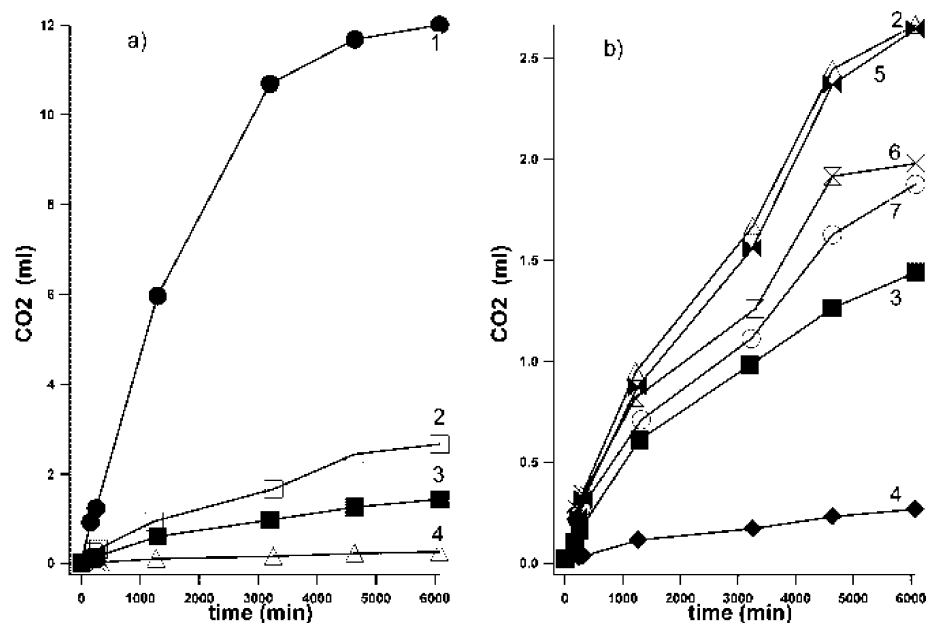

Figure 11. TiO$_2$ Degussa P-25, under full Suntest lamp irradiation, no filter at $\lambda > 410$ nm. Kinetics of double bond index formation for (1) Degussa P-25 under full Suntest light, (2) S$-$TiO$_2$ 500 $\times$ 2, $\lambda > 410$ nm, (3) S$-$TiO$_2$ 350 $\times$ 3, $\lambda > 410$ nm, (4) S$-$TiO$_2$ 400 $\times$ 8, $\lambda > 410$ nm, (5); S$-$TiO$_2$ 500 $\times$ 5, $\lambda > 410$ nm, (6) Degussa P-25, $\lambda > 410$ nm, and (7) S$-$TiO$_2$ 900 $\times$ 1, $\lambda > 410$ nm.

1. This is the initiation step in the chain radical oxidation of PE in the presence of oxygen. The origin of the color observed for the N$-$ and S$-$TiO$_2$ is due to the narrowing of the band gap with the formation of isolated narrow bands above the valence band, and possibly due to the formation of manifold surface states. Asahi et al.[4,6] calculated the band structure of TiO$_{2-x}$N$_x$ where oxygen sites were substituted by nitrogen and reported that the mixing of the N2p and O2p orbitals narrowed the band gap. S-doping of rutile by ion implantation has been reported to lead to the reduction of the band gap. Umebayashi et al.[13] calculated the band structure of doped TiO$_2$ where oxygen sites are substituted by S atoms. The mixing of the S3p states with the valence band was found to contribute to an increase in the valence bandwidth leading to band gap narrowing in the S-doped TiO$_2$. Both theories about the band gap narrowing either by the N or S substitution for oxygen are in qualitative

agreement with the formation of the color in TiO$_2$ after urea or thiourea treatment. In ref 1, the narrowing of the band gap in the N-doped TiO$_2$ was not reported. A small narrowing of the band gap of about 20 meV was reported for N-doped TiO$_2$ in ref 16. Recently, the position of the valence band was reported to remain unchanged upon nitrogen doping.[16] From the data in Table 3, it can be seen that for S$-$ and N$-$TiO$_2$ samples, the narrowing of the band gap varied for different samples from 0 to 530 mV. The samples with the vivid yellow color display a lower band gap value as determined from optical measurements. The samples with the pale yellow color have E_g values close to the undoped TiO$_2$. For colored samples the absorbance in the visible obeys Urbach's law in the diapason of about 1$-$1.5 octave. This suggests that color formation is due to states introduced in the band gap due to the doping. Taking into account the similarity of the DRS spectral of the N$-$ and

Figure 12. (a) Kinetics of CO_2 evolution during the photocatalytic oxidation of PE by $S-TiO_2$. Comparison between the PE oxidation with Degussa P-25 under entire full Suntest irradiation and the with PE oxidation under $\lambda > 410$ nm: (1) Degussa P-25, under full Suntest irradiation; (2) $S-TiO_2$ 400 × 8, $\lambda > 410$ nm; (3) Degussa P-25, $\lambda > 410$ nm; (4) $S-TiO_2$ 900 × 1, $\lambda > 410$ nm; (5) $S-TiO_2$ 350 × 2, $\lambda > 410$ nm; (6) $S-TiO_2$ 500 × 5, $\lambda > 410$ nm; (7) $S-TiO_2$ 500 × 2, $\lambda > 410$ nm. (b) PE oxidation under $\lambda > 410$ nm. The meaning of the traces 2-7 is the same as in (a).

$S-TiO_2$ samples, common states can be suggested for the N- and S-doped samples. We suggest that new states form in the vicinity of oxygen-deficient sites in the band gap. These states induce activity in the visible and N- or S-doping seem to hinder reoxidation.[3] The assumption about the oxygen deficient centers agrees with the band shift and widening observed in the Raman spectra of $S-TiO_2$ samples.

Conclusions

The TiO_2 powders with visible absorption were obtained by using sol–gel techniques followed by calcinations in the presence of thiourea or urea. For the ground samples, TiO_2 was mixed with thiourea followed by annealing. Elemental analyses show the presence of 1 mol % N for $N-TiO_2$ and ~1.5 mol % S for $S-TiO_2$ samples, respectively.

XRD measurements show that the crystalline phase in the active doped samples was anatase. ATR-FTIR measurements presented the evidence for the existence of SO_4^- bands in the samples prepared with thiourea. These bands can be removed by thoroughly washing the sample.

DRS spectra of the $S-$ and $N-TiO_2$ samples reveal similar features. This suggest similar centers in TiO_2 due to either N- or S-doping. The treatment of the DRS spectra according to the theory of indirect allowed optical transitions gives values for the band gap which coincide with or are slightly narrower than the band gap of anatase. The narrowing of the E_g band was observed for the vivid yellow samples but was negligibly small for the pale yellow samples. The dependence of the absorption vs photon energy for the shoulder inherent to the TiO_2 spectra followed Urbach's law dependency in the 1–1.5 octave. For $S-$ and $N-TiO_2$ samples the energy distribution of states prepared by sol–gel were close to 377 and 334 mV, respectively, as observed from the DRS spectra.

The N_2 adsorption–desorption isotherms showed a different porosity for the samples investigated. The sol–gel sample presented a wider hysteresis loop evidencing a higher pore order

structure. The samples obtained by the grinding technique present a weaker hysteresis loop.

The dynamics of the transient decay presented a nonexponential form after the excitation with laser pulses at $\lambda = 354$ nm. The half-life of the transient decay for the different samples varied between 0.5 and 1.5 μs. Similar half-lives were observed for nondoped TiO_2 samples. Because the transient arises due to the electron in the conduction band, the lack of a meaningful correlation between the transient decay and the N- and S-doping level of TiO_2 suggests the lack of acceleration of the electron decay relative to the undoped TiO_2 samples in the sub-microsecond region.

$S-TiO_2$ mediated photocatalytic peroxidation of the phosphatydilethanol amine (PE) from the brain bovine occurs under light $\lambda > 410$ nm. This peroxidation was monitored by the formation of conjugate double bonds. CO_2 formation was also followed during the course of these experiments.

References and Notes

(1) Irie, H.; Watanabe, Y.; Hashimoto, K. *J. Phys. Chem. B* **2003**, *107*, 5483–5486.

(2) Irie, H.; Watanabe, Y.; Hashimoto, K. *Chem. Lett.* **2003**, *32*, 772–773.

(3) Ihara, T.; Miyoshi, M.; Iriyama, Y.; Matsumoto, O.; Sugihara, S. *Appl. Catal. B–Environ.* **2003**, *42*, 403–409.

(4) Asahi, R.; Morikawa, T.; Ohwaki, T.; Aoki, K.; Taga, Y. *Science* **2001**, *293*, 269–271.

(5) Asahi, R.; Morikawa, T.; Ohwaki, T.; Aoki, K.; Taga, Y. *Science* **2002**, *295*, 627–627.

(6) Morikawa, T.; Asahi, R.; Ohwaki, T.; Aoki, K.; Taga, Y. *Jpn. J. Appl. Phys. Part 2–Lett.* **2001**, *40*, L561–L563.

(7) Ohno, T.; Mitsui, T.; Matsumura, M. *Chem. Lett.* **2003**, *32*, 364–365.

(8) Ohno, T. *Water Sci. Technol.* **2004**, *49*, 159–163.

Doped TiO$_2$ in the Peroxidation of Biomolecules

J. Phys. Chem. B, Vol. 109, No. 12, 2005 **6003**

(9) Ohno, T.; Akiyoshi, M.; Umebayashi, T.; Asai, K.; Mitsui, T.; Matsumura, M. *Appl. Catal. A—General* **2004**, *265*, 115−121.

(10) Zhu, J. F.; Zheng, W.; Bin, H. E.; Zhang, J. L.; Anpo, M. *J. Mol. Catal. A—Chem.* **2004**, *216*, 35−43.

(11) Trapalis, C. C.; Keivanidis, P.; Kordas, G.; Zaharescu, M.; Crisan, M.; Szatvanyi, A.; Gartner, M. *Thin Solid Films* **2003**, *433*, 186−190.

(12) Amezaga-Madrid, P.; Nevarez-Moorillon, G. V.; Orrantia-Borunda, E.; Miki-Yoshida, M. *FEMS Microbiol. Lett.* **2002**, *211*, 183−188.

(13) Umebayashi, T.; Yamaki, T.; Yamamoto, S.; Miyashita, A.; Tanaka, S.; Sumita, T.; Asai, K. *J. Appl. Phys.* **2003**, *93*, 5156−5160.

(14) Ihara, T.; Miyoshi, M.; Ando, M.; Sugihara, S.; Iriyama, Y. *J. Mater. Sci.* **2001**, *36*, 4201−4207.

(15) Shanmugasundaram, S.; Kisch, H. *Angew. Chem. Int. Ed.* **2003**, *42*, 4908−4911.

(16) Shanmugasundaram, S.; Kisch, H. *ChemPhysChem* **2003**, *4*, 487−490.

(17) Umebayashi, T.; Yamaki, T.; Tanaka, S.; Asai, K. *Chem. Lett.* **2003**, *32*, 330−331.

(18) Ohno, T.; Tsubota, T.; Nishijuma, K.; Miyamoto, Z. *Chem. Lett.* **2004**, *33*, 750−751.

(19) Wolfrum, E. J.; Huang, J.; Blake, D. M.; Maness, P. C.; Huang, Z.; Fiest, J.; Jacoby, W. A. *Environ. Sci. Technol.* **2002**, *36*, 3412−3419.

(20) Saito, T.; Iwase, T.; Horie, J.; Morioka, T. *J. Photochem. Photobiol. B—Biol.* **1992**, *14*, 369−379.

(21) Sunada, K.; Kikuchi, Y.; Hashimoto, K.; Fujishima, A. *Environ. Sci. Technol.* **1998**, *32*, 726−728.

(22) Sunada, K.; Watanabe, T.; Hashimoto, K. *J. Photochem. Photobiol. A—Chem.* **2003**, *156*, 227−233.

(23) Blake, D. M.; Maness, P. C.; Huang, Z.; Wolfrum, E. J.; Huang, J.; Jacoby, W. A. *Sep. Purif. Methods* **1999**, *28*, 1−50.

(24) Nadtochenko, V. A.; Rincon, A. G.; Stanka, S. E.; Kiwi, J. *Photochem. Photobiol. A.: Chem.* **2004**, *169*, 133−137.

(25) Huijbesgts, R. H.; de Kroon A. I. P. M.; de Kuijff, B. *Biochim. Biophys. Acta* **2000**, *1469*, 43.

(26) Kubelka, P.; Munk, F. *Z. Technol. Phys.* **1931**, *12*, 593.

(27) Bersani, P.; Lottic, P.; Xing-Zhao D. *Appl. Phys. Lett.* **1998**, *72* (1), 73−75

(28) Parker, C. J.; Siegel, R. W. *Appl. Phys. Lett.* **1990**, *57* (9), 943−945.

(29) Barret, P. E.; Joyner, L. G.; Halenda, P. H. *J. Am. Chem. Soc.* **1951**, *73*, 373−382.

(30) Smith, R. A. *Semiconductors*, 2nd. ed.; Cambridge University Press: Cambridge, U.K., 1978.

(31) Tang, H.; Prasad, K.; Sanjines, R.; Schmid, P. E.; Levy, F. *J. Appl. Phys.* **1994**, *75*, 2042−2047.

(32) Skinner, D. E.; Colombo, D. P., Jr.; Cavaleri, J. J.; Bowman, R. M. *J. Phys. Chem.* **1995**, *99*, 7853−7859.

(33) Kinder, R.; Ziegler, C.; Wessels, J. M. *Int. J. Radiat. Biol.* **1997**, *71*, 561−571.

(34) Kim, W. T.; Kim, C. D.; Choi, H. C. *Phys. Rev. B* **1984**, *30*, 3625−3628.

(35) Kim, W. T. *Phys. Rev. B* **1983**, *28*, 6529−6531.